



Delft University of Technology

A Comprehensive Workflow for High Resolution 3D Solar Photovoltaic Potential Mapping in Dense Urban Environment

A Case Study on Campus of Delft University of Technology

Zhou, Yilong; Verkou, Maarten; Zeman, Miro; Ziar, Hesam; Isabella, Olindo

DOI

[10.1002/solr.202100478](https://doi.org/10.1002/solr.202100478)

Publication date

2021

Document Version

Final published version

Published in

Solar RRL

Citation (APA)

Zhou, Y., Verkou, M., Zeman, M., Ziar, H., & Isabella, O. (2021). A Comprehensive Workflow for High Resolution 3D Solar Photovoltaic Potential Mapping in Dense Urban Environment: A Case Study on Campus of Delft University of Technology. *Solar RRL*, 6(5), Article 2100478. <https://doi.org/10.1002/solr.202100478>

Important note

To cite this publication, please use the final published version (if applicable). Please check the document version above.

Copyright

Other than for strictly personal use, it is not permitted to download, forward or distribute the text or part of it, without the consent of the author(s) and/or copyright holder(s), unless the work is under an open content license such as Creative Commons.

Takedown policy

Please contact us and provide details if you believe this document breaches copyrights. We will remove access to the work immediately and investigate your claim.

A Comprehensive Workflow for High Resolution 3D Solar Photovoltaic Potential Mapping in Dense Urban Environment: A Case Study on Campus of Delft University of Technology

Yilong Zhou, Maarten Verkou, Miro Zeman, Hesam Ziar,* and Olindo Isabella

Photovoltaic (PV) technology is the most promising renewable energy source to be integrated on urban building surfaces. Modeling and simulating urban PV systems pose more challenges than the conventional ones installed in open field due to rich urban morphology. Herein, a comprehensive workflow to estimate urban solar PV potential is developed where TU Delft campus is used as a case study. This workflow only requires light detection and ranging data and building footprints as data inputs, and multiple levels of result can be delivered including accurate geo-referenced 3D building models, annual solar irradiation map, annual DC/AC yield maps and classified roof segments according to the specific yield of mounted PV system. The study reports a total of $\approx 8.1 \text{ GWh year}^{-1}$ of PV energy which can be collected from campus building roofs and facades. Given the total electricity demand on the entire campus being 82.6 GWh/year , this PV potential can cover roughly 10% of the current electricity demand. The results constitute an initial assessment of solar PV potential on TU Delft campus buildings that is currently being used to prioritize PV integration on buildings and accelerate the transition toward a climate-neutral campus.

a boost of green energy penetration in the energy system is required.

Current energy distribution system is predominantly featured with centralized generator and monodirectional distribution network. This means that electricity is mainly produced in a giant power plant and transported through long-distance cables to reach consumer end. Unfortunately, the green future scenario cannot be simply achieved by replacing the conventional power plants with large green energy farms. One of the reasons lies in the fact that centralized paradigm lacks reliability because the entire grid can fail with the failure in central power plant.^[3] Considering the intermittent nature of renewable energies, optimizing the energy system reliability will be even more challenging. Another argument against centralization is the power loss during long-distance


transportation and distribution of electricity.^[4] As a solution, decentralized green energy sources allow one to produce electricity locally. It distributes the responsibility of electricity generation over small-sized producers, and power loss as a result of transmission can also be effectively minimized because the generator is either on site or near-site. Meanwhile, given the fact that the majority people will be living in densely populated cities in the future,^[5] developing decentralized renewable energy sources in urban environment will play a major role in the green energy transition.

Delft University of Technology (TU Delft) is aiming for a climate-neutral campus by 2030.^[6] Of all the renewable energy sources, photovoltaic (PV) is the most promising technology to fulfil this target. It can be integrated with most urban elements such as buildings,^[7] roads,^[8] and waterways,^[9] without demanding additional urban space.^[10] Currently, only 1.2 MWp of solar capacity is installed on campus buildings.^[11] To reach TU Delft ambitious goal, the number of mounted PV panels needs to be drastically increased such that 50% of electricity generation on campus can be covered. Although PV technology is preferred due to its high compatibility, designing PV system in the urban environment is no easy task. Densely constructed cities restrict the incoming sunlight, and rich urban morphology including buildings, infrastructures and vegetations can cause complex shading patterns. Therefore, it is fundamental to understand the urban context such that available building surfaces can be

1. Introduction

The Paris Agreement released in 2015 states that the global warming should be limited to 1.5°C .^[1] In response to this agreement, the Dutch government issued the National Climate Agreement in 2019, and an ambitious goal was established where by 2030 the greenhouse gas emission must be reduced by 49% compared to 1990 levels.^[2] It is also expected that 70% of the electricity generation will be covered by renewable energy sources by 2030 and become fully sustainable by 2050. To achieve this goal,

Y. Zhou, M. Verkou, M. Zeman, H. Ziar, O. Isabella
Photovoltaic Materials and Devices group
Delft University of Technology
Mekelweg 4, Delft 2628CD, The Netherlands
E-mail: H.Ziar@tudelft.nl

 The ORCID identification number(s) for the author(s) of this article can be found under <https://doi.org/10.1002/solr.202100478>.

© 2021 The Authors. Solar RRL published by Wiley-VCH GmbH. This is an open access article under the terms of the Creative Commons Attribution-NonCommercial-NoDerivs License, which permits use and distribution in any medium, provided the original work is properly cited, the use is non-commercial and no modifications or adaptations are made.

DOI: 10.1002/solr.202100478

identified and their PV potential can be assessed.^[12,13] One possible way is by using aerial images where image recognition is implemented to identify the geometry of suitable roof surfaces for PV integration.^[14–16] Among others, orthographic aerial images provide the single perspective of an area of buildings, and the height of buildings is generally estimated by fitting a normal distribution function; while aerial stereo images allow the generation of digital surface model (DSM) from stereophotogrammetry by using overlapping images taken from different positions.^[17] Another approach is based on light detection and ranging (LiDAR) which is currently most widely used spatial data to represent and reconstruct the urban environment.^[18] This remote sensing technology is able to densely sample the surface of the earth by transmitting laser light toward earth surface and analyzing the reflected signals.^[19] The management and analysis of these spatial data are performed with geographic information system (GIS). It offers a variety of GIS tools to help users process the spatial data which contributes to the determination of building surface candidates suitable for PV integration.^[20] Apart from understanding the territory, the implemented model should also deliver an accurate solar PV potential calculation result without demanding heavy computational cost.

Generally, studying the potential of renewable energies such as solar energy can be approached in a hierarchical manner: 1) physical potential which represents the total amount of solar irradiation impinging on the study area; 2) geographical potential which considers only the solar irradiation on surfaces that are available for PV integration; 3) technical potential where technical performance of certain type(s) of PV technology is further taken into account; and finally iv) economic potential which assesses the financial feasibility of the PV system installation.^[21] In recent decades, multiple studies have been carried out on the estimation of urban solar energy.^[14,15,22–26] Depending on the project objective and the availability of data source, the results are delivered to one of the aforementioned hierarchies. Jaroslav et al.^[27] assessed the PV potential in a small city in eastern Slovakia by using open-source tools. They start with the creation of 3D city model, and use r.sun solar radiation model and PVGIS to calculate roof technical potential. Santos et al.^[28] also proposed a two-stage process where in addition to the incoming solar energy, the population distribution at building level is also modelled. But both works only studied the building roof surfaces, and the shadings imposed by trees, infrastructures, and artifacts were not taken into account. Catita et al.^[29] extended the solar potential analysis to vertical building facades by means of hyperpoints. Each hyperpoint contains a set of points which share XY coordinates but have different Z values. This approach realized a 3D mapping of solar potential on building surfaces, but more in-depth result such as geographical or technical potential was not delivered. Similar works have been done by Brito et al.^[26] on city of Lisbon and Vulkan et al.^[30] on a neighborhood of Rishon LeZion in Israel. Both works based their analysis on a relatively low spatial resolution (1 by 1 m²), and only the physical potential on building surfaces is calculated. Particularly in the work from Vulkan, small-scale artifacts are excluded, and the solar irradiation calculation only considers direct component. Vo et al.^[31] reported a complete workflow to estimate in detail the urban solar potential by processing each LiDAR point, but this per-point analysis is computationally heavy and requires a LiDAR dataset with high resolution (300 points m⁻²). Another numerical

model (PLANTING) for solar PV potential estimation is developed by Murshed et al.^[32] where economical potential on building roofs and facades can be delivered. However, this approach is also time consuming because the analysis is conducted on an hourly basis, and it requires semantically and topologically correct CityGML data which are generally difficult to prepare.

Therefore, the aim of this work is to develop a large-scale urban PV AC yield modeling workflow based on the minimum amount of freely available input datasets. In this article, we presented such workflow where only LiDAR data and building footprints are required as inputs. To the authors' knowledge, this is not the case in other literatures where additional input dataset is needed such as aerial images,^[15] or expensive 3D building models need to be available.^[33,34] Meanwhile, the workflow is able to deliver PV AC yield for both building roofs and facades which provides the decision makers more insights on urban solar plan than the works which only consider PV AC yield for rooftops,^[25] or solar potential on building surfaces.^[26] Particularly, compared to the work presented by de Vries et al.^[15] where module fitting is also implemented, our workflow further investigated: 1) portrait and dual-tilt mounting configurations on flat roofs; 2) partial shading losses induced by mutual shading; 3) skyline variation for each module; and 4) dynamic inverter efficiency based on Sandia National Laboratories (SNL) model. In the work done by Freitas et al.,^[35] the state-of-the-art solar radiation models have been discussed. Most of them calculate the hourly irradiance received on the plane of array (PoA) and integrate the results over the year to obtain the annual solar irradiation. Such repetitive calculation significantly increases the computational time in a large-scale urban PV potential scan. In this work, our in-house developed simplified skyline-based model is used to map the solar PV potential for TU Delft campus.^[36] This model can offer accurate estimation on annual solar PV potential on a surface whereas the computational demand is substantially reduced.

The rest of paper can be broken down into following parts: Section 2 describes all the steps of this methodology. As a demonstration, the result of one building from each step is presented. In Section 3, the numerical solar PV potential result of the demonstration building is discussed, and the solar irradiation map of all the buildings on TU Delft campus is shown. The hyperlink to a web map is also provided which visualizes all the simulation results in this work. The validation study is conducted in Section 4, and the limitations of this methodology as well as future research works are discussed in Section 5. Lastly conclusions are drawn in Section 6.

2. Methodology

This section describes the utilized methodology for solar PV potential mapping in a large-scale urban area. This is a universal approach which only requires LiDAR data and building footprints as inputs as shown in **Figure 1**. Main steps include 1) reconstruction of 3D building models; 2) annual solar irradiation map generation on building surfaces; 3) annual DC yield map generation on building surfaces; 4) annual AC yield map generation on building surfaces; and 5) roof segment classification based on the specific yield of mounted PV system. Each step is explained in detail in its corresponding section.

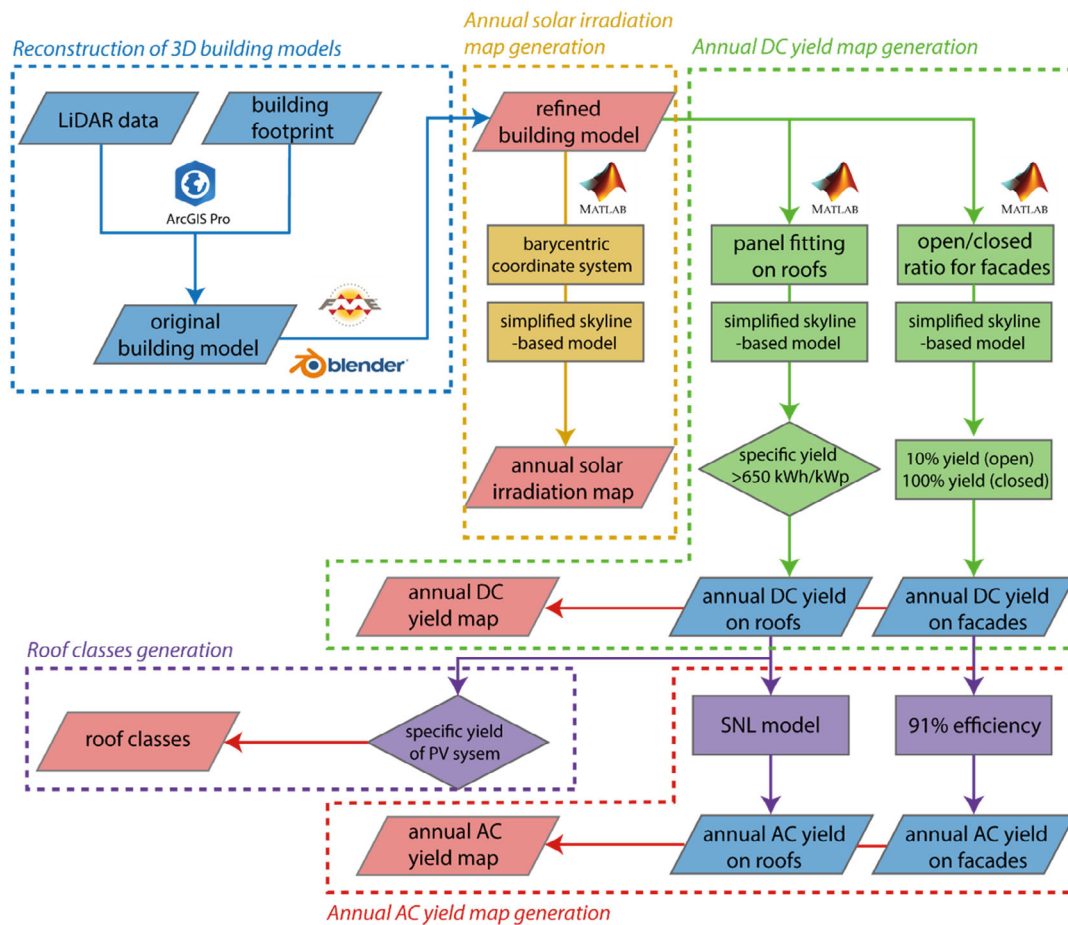


Figure 1. Workflow of the developed methodology. The final results are the ones in the red parallelogram, and each dashed box represents the processes required to achieve each result.

2.1. Reconstruction of 3D Building Model

One of the key factors to accurately estimate the solar PV potential of urban PV system is to reconstruct high-quality 3D building models.^[28,29,37] Airborne LiDAR data is increasingly used to serve this purpose because it provides detailed geographical and topological information.

When LiDAR data is being collected, laser light is sent from the device on the drone toward the earth surface. As the light travels to the ground, it reflects off from the objects. This reflected light returns to the sensor and gets recorded. By analyzing the time that light travels to the ground and back from the objects, one can calculate the distance which is further converted to elevation.^[38] LiDAR technology can also distinguish trees from other objects. As the laser light traverses through trees, the photons can be partially reflected by branches or leaves since they are small in size and are full of gaps. The remaining photons continue their journey until they get fully reflected. Thus, multiple returns can be captured and recorded by the sensor from one pulse of light.^[19] The Dutch government collected the first batch of LiDAR data (AHN1) in 1997, and the latest accessible version (AHN3) was released in 2019.^[39] Generally,

the time span of LiDAR acquisition stretches over a few years. The AHN3 data was collected between 2014 and 2019, and it has a resolution of around 6 to 10 points per square meter. The data of Delft was collected in 2014 and has a lower resolution of 3 to 5 points per square meter.^[40]

The reconstruction of 3D building models is based on building footprint and LiDAR data.^[41] These two datasets are provided by the Dutch government and are freely available. The building footprint is the outer edge of the outside walls of the building which represents the planimetric confinement of building layout. To better demonstrate the workflow, the building of Electrical Engineering, Mathematics and Computer Science (EEMCS) faculty is used as a case study whose building footprint and LiDAR data are shown in **Figure 2**.

First, the original building models are generated in ArcGIS Pro with LAS Building Multipatch tool.^[42] It reconstructs the building models in a way that a network of triangular meshes is derived by connecting all the adjacent LiDAR points found inside the building footprint. **Figure 3** shows the original 3D building model of EEMCS faculty. It can be observed that the building model is made up of a number of triangular meshes which cover the entire building model surface. Due to the bumpiness of the original LiDAR data, adjacent triangular meshes

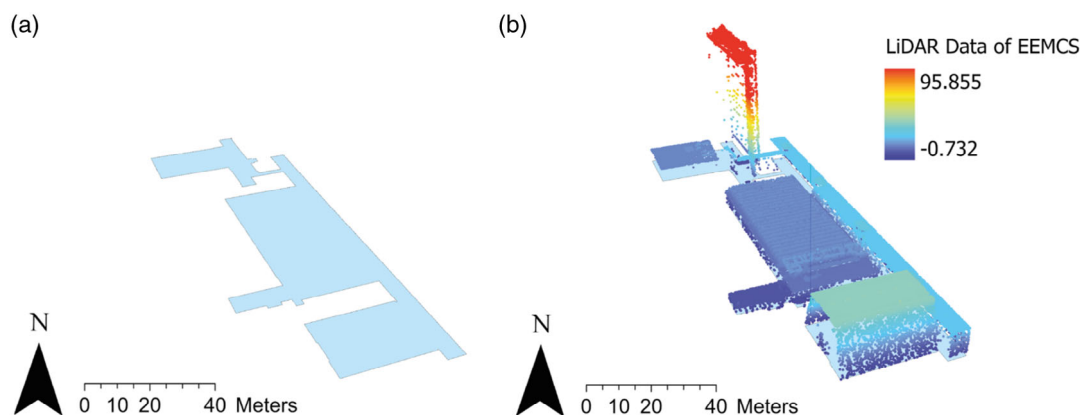


Figure 2. a) Building footprint of the building of EEMCS faculty; b) LiDAR data of the building of EEMCS faculty along with their height in meters.

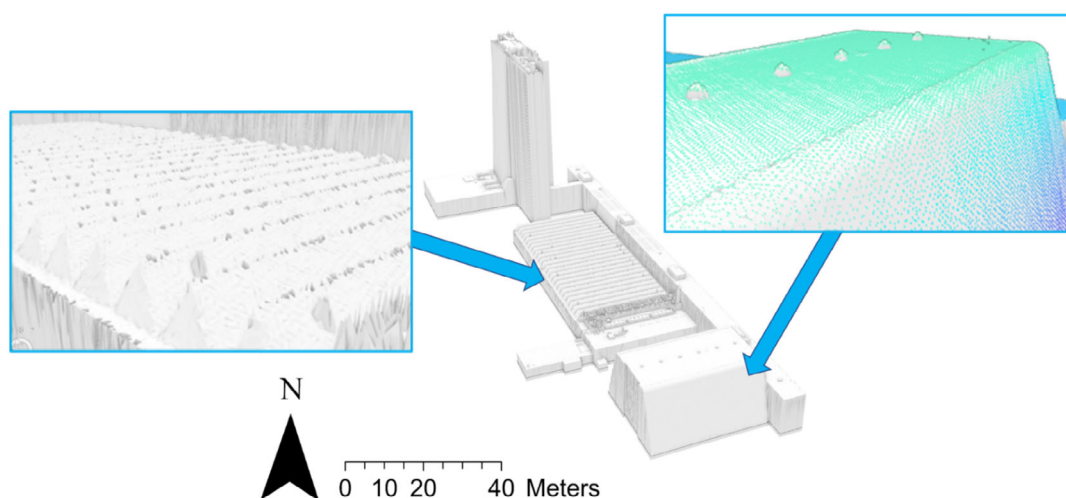


Figure 3. The original 3D building model of building of EEMCS faculty where building surfaces are made up of triangular meshes.

within a roof segment might not be aligned, leading to large discrepancy in terms of slope and orientation which ultimately degrades the fidelity of solar PV potential simulation results. Thus, the geometry must be refined such that accurate models can be passed in for further analysis.

To do this, a free 3D creation suite named Blender is used. Its built-in mesh simplification tool allows users to remove unnecessary vertices or meshes with minimum changes to the model shape.^[43] After running this tool for multiple rounds, the number of vertices and meshes is reduced to only 1% of that of the original building model. A comparison of the building model of EEMCS faculty before and after mesh simplification is presented in **Figure 4**. It is clear that the number of meshes is drastically reduced while the shape of the building is still well maintained.

The final building model is obtained by manual adjustments to remove the outliers and align the edges. **Figure 5** presents the refined EEMCS building model. By zooming into various parts of the model, one can see that only fundamental roof and facade polygons are included. It is worth noting that all the building artifacts such as ventilation system, antennas, and chimneys are manually excluded because they do not contribute to the feasible

area for PV installation. Depending on the complexity of the building, the time it requires for our semiautomatic method to reconstruct geo-referenced building models ranges from some minutes to a couple of hours. This removes considerable amount of time for manual building model reconstruction using software such as SketchUp which generally requires detailed building floor plan and several days of work to reconstruct one building model.^[44,45] Compared to another building model recreation approach where drone based photogrammetry is used, our method requires neither traveling nor drone operation skills, but it can still deliver highly accurate geo-referenced building models because the only inputs are LiDAR data and building footprints which are both freely available.^[46]

One of the main limitations of this methodology is that the building façade details cannot be properly modelled as shown in **Figure 6**. The aperture at the top of high-rise building is not reflected on the building model. Meanwhile, the open space at the bottom of low rise is also not properly mapped. This is mainly due to the lack of digital façade information, and the location information of windows, ledges, or gaps is generally not available from the LiDAR data. Therefore, only sharp closed

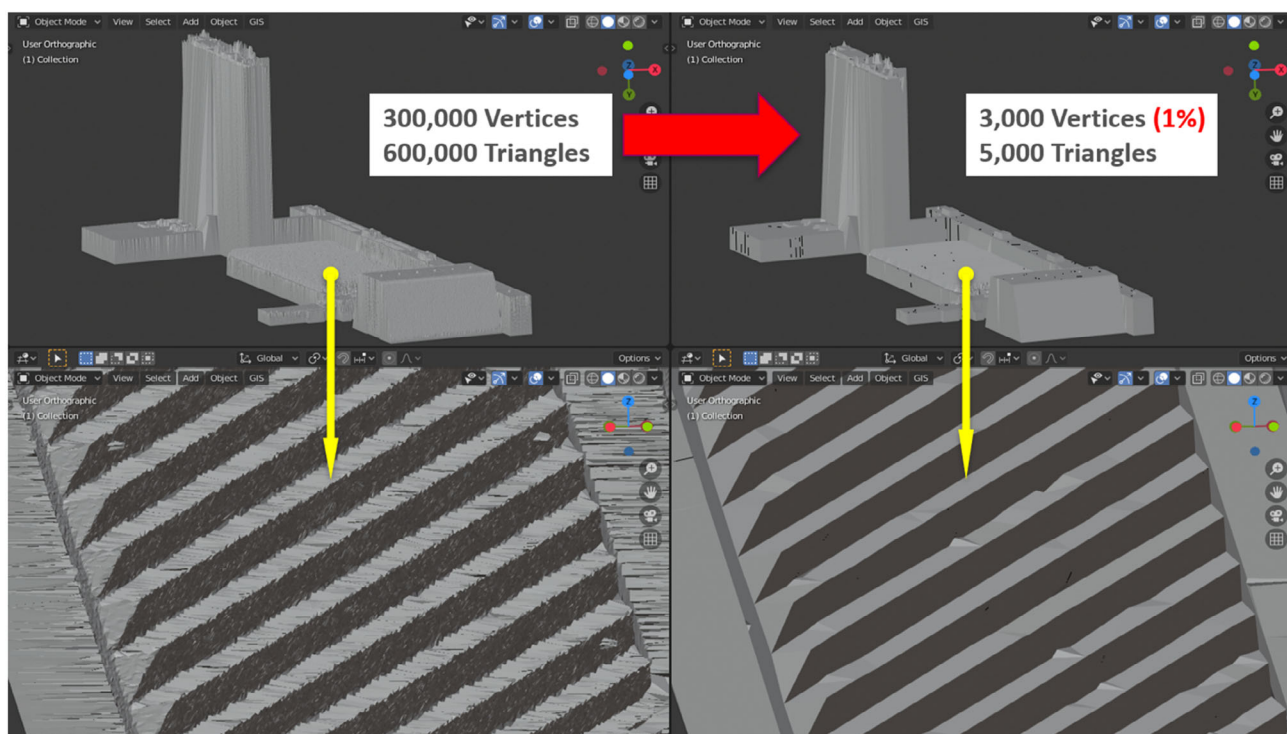


Figure 4. Building model of EEMCS faculty before and after mesh simplification where the number of vertices and triangles is reduced to 1% of that of the original building model.

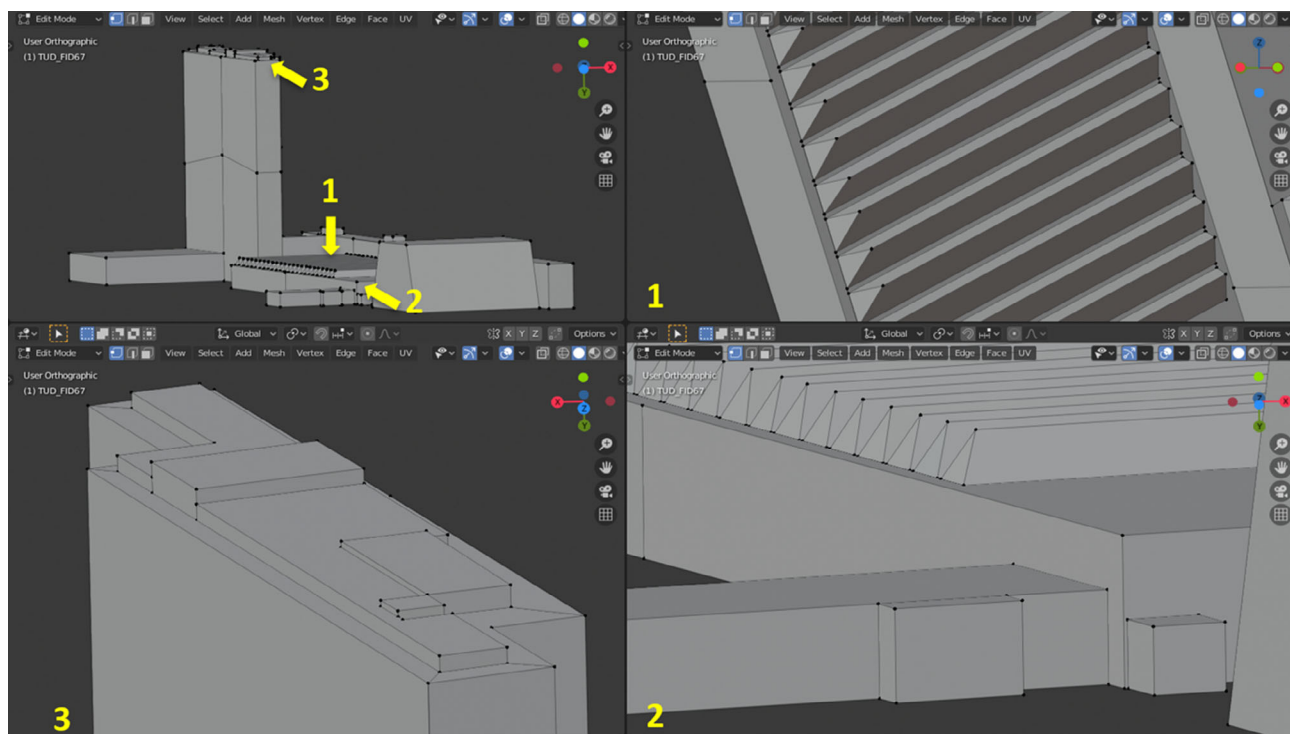


Figure 5. The final refined building model of EEMCS faculty where only necessary roof and facade polygons are included.

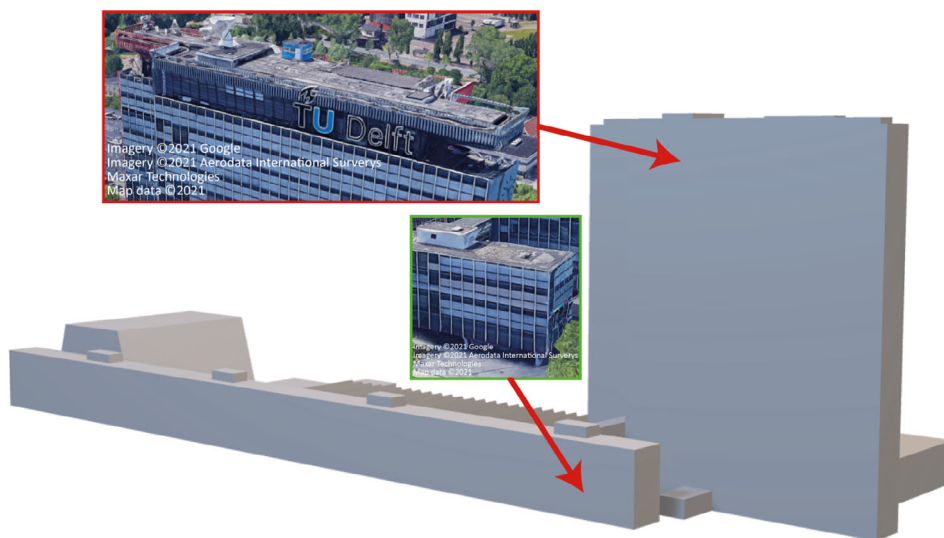


Figure 6. Limitation of the 3D building model reconstruction workflow where the building facade cannot be properly recreated due to the lack of facade information. The aerial photo is obtained from GoogleMap.

facades are reconstructed by connecting the roof edges with the building footprint.

2.2. Annual Solar Irradiation Mapping

To map the annual solar irradiation, the first step is to generate a uniformly distributed grid on the building surface. Each point in this grid represents a specific surface area whose incident solar irradiation can be calculated with the simplified skyline-based model.^[36] The surface area each point occupies is determined by the grid density. For instance, a grid of 0.5 m means that each point covers an area of 0.25 m². The generation of surface grid is based on barycentric coordinate system where the location of any point within a triangle can be expressed by the following formula^[47,48]

$$P = \alpha \cdot A + \beta \cdot B + \gamma \cdot C \quad (2.1)$$

where P is the coordinate of the point of interest. A , B , and C are the coordinates of triangle vertices. To keep the point of interest within the triangle, the following constraints must be met

$$\begin{cases} \alpha, \beta, \gamma \in [0, 1] \\ \alpha + \beta + \gamma = 1 \end{cases} \quad (2.2)$$

The generation of a uniformly distributed grid on the building surface requires manipulation of the area of triangles subdivided by the point of interest. **Figure 7** illustrates how the barycentric coordinate system is applied to determine the location of point P . In the figure, point P subdivides the original triangle into 3 sub-triangles, and the factors α , β , and γ can be determined by calculating the ratio between the area of the subtriangle and the area of the original one. As an example, factor alpha can be determined by dividing the area of blue triangle by that of the original one. The rest can be done in the same way. The manipulation of triangle area ratio allows one to map an evenly distributed grid on

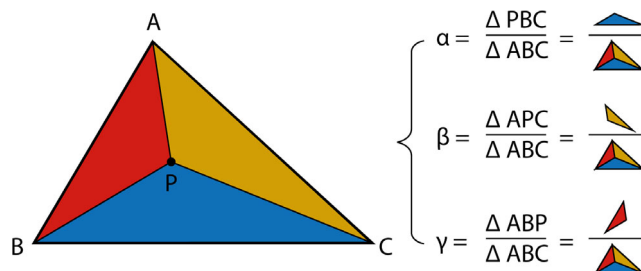


Figure 7. Using barycentric coordinate system to manipulate the location of the points where point P is the point of interest and it subdivides the original triangle into three small triangles.

building surfaces with desired grid size. In this work, a grid size of 0.5 m is selected. **Figure 8** shows the outcome after implementing barycentric coordinate system on one of the facades of the building of EEMCS faculty. It is clear in the zoomed image that the points are uniformly distributed on the facade surface with a gap of 0.5 m.

The annual solar irradiation is calculated per point with the simplified skyline-based model.^[36] This model uses a set of synthetic skylines to curve fit a polynomial function that has five coefficients and two main parameters of SVF and sun coverage factor (SCF), where SCF is the representative of if the sun is blocked by the horizon or not, and SVF is how much of the sky hemisphere is freely visible. This set of five coefficients is unique for every tilt and orientation under one climate regardless of the geometry. Here the local climate in Delft, the Netherlands is used to calculate these five coefficients for every 45° azimuth and 5° tilt angle (the degrees in between are linearly interpolated). The two indicators (SVF and SCF) can be derived from the skyline profile by using our in house developed HorizonScanner MATLAB script.^[49] This script constructs the skyline for any point with arbitrary tilt and azimuth angle by scanning the DSM. For any observer point of interest, it splits

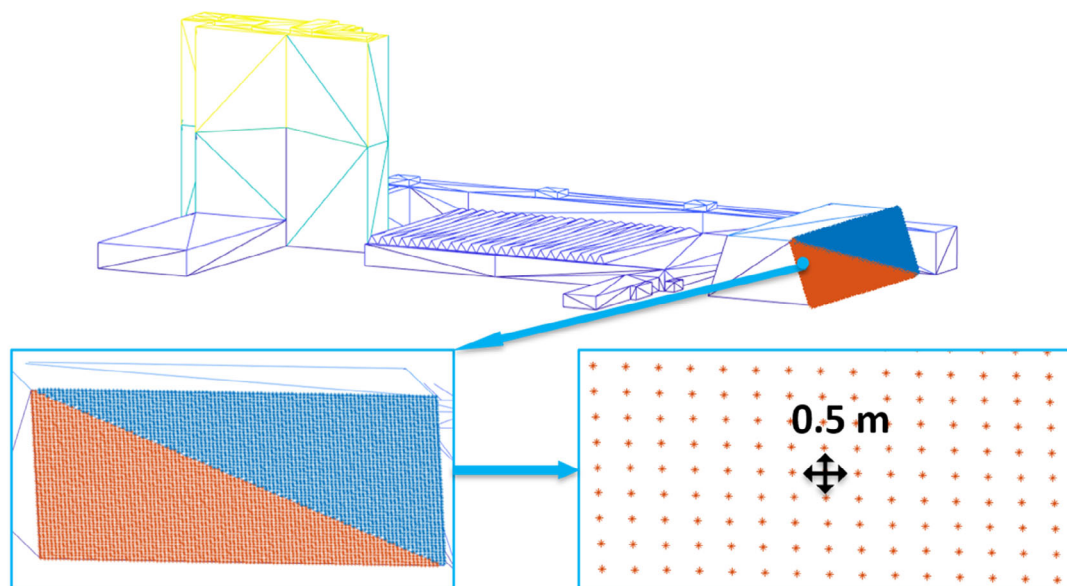


Figure 8. A grid with a density of 0.5 m is generated with barycentric coordinate system on one of the facades of the building of EEMCS faculty.

up the full azimuth range into several slices and check all the height points lie within this slice. The height of the point with the largest altitude angle is assigned as the horizon altitude for that azimuth slice. The tilt and azimuth angle of building surface are derived from the face normal vector as shown in **Figure 9**. Roof tilt θ_R is found as the angle between the face normal n_R and the ground normal $[0,0,1]$, while roof azimuth A_R can be obtained by calculating the angle between due North vector $[0,1,0]$ and the projection of face normal on the ground plane. **Figure 10** shows the solar irradiation map of EEMCS faculty building from bird view. Although the rooftop artifacts are excluded in the building model reconstruction phase, the solar potential assessment still takes into account the shadings imposed by them because the skyline profile is extracted from the DSM of raw LiDAR data. These obstacles limit the incoming sunlight such that the roof sections receive lower solar irradiation and they are displayed in dark red color. By comparing the solar irradiation map with the GoogleMap aerial photo, one can

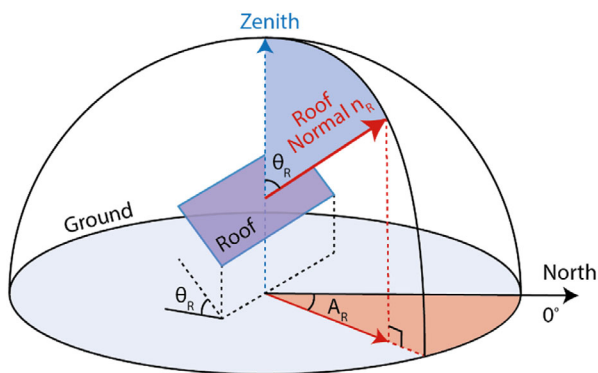


Figure 9. Calculation of roof tilt θ_R and azimuth A_R from roof surface normal n_R .

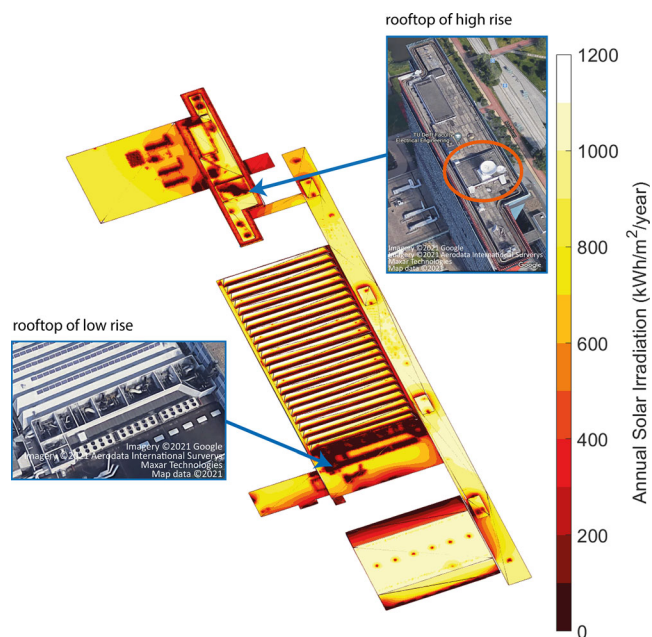


Figure 10. Annual solar irradiation map of the building of EEMCS faculty from bird view where the aerial photos are obtained from GoogleMap.

quickly identify the type of obstacles. For instance, rooftop of the high rise of EEMCS faculty building is shaded by the antennas, and the rooftop of low-rise building is shaded by the ventilation system. In addition to the shadings caused by obstacles of the building itself, the surrounding urban context can also restrict the amount of irradiation impinging on the building surface. **Figure 11** shows the solar irradiation map of EEMCS faculty building from side view. It is evident that the southern facade of the high-voltage lab is subject to significant shading at its bottom

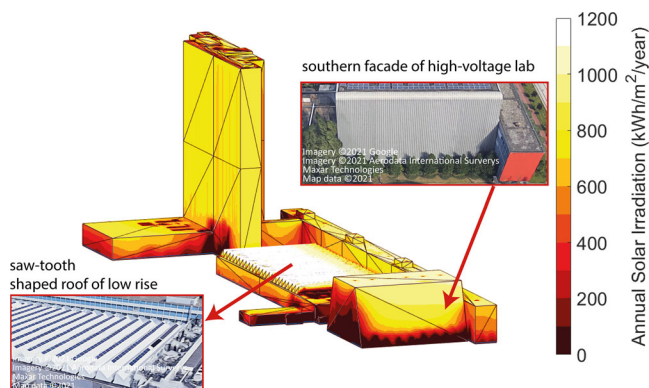


Figure 11. Annual solar irradiation map of the building of EEMCS faculty from side view where the aerial photo is obtained from GoogleMap.

region due to the trees at the front. Meanwhile, it can also be concluded that the saw-tooth shaped rooftop of low rise receives the highest annual solar irradiation where a high PV yield can be expected.

2.3. Annual DC Yield Mapping

The annual solar irradiation map provides the information on physical potential that building surfaces possess. Directly using

the same grid points to calculate DC yield results in an overestimation of what the PV systems actually can deliver. One reason lies in the fact that parts of the roof surfaces are not suitable for PV module installation. These can either be the locations that are already occupied by rooftop artifacts, or the spots where installation of PV system is not financially feasible given the current price of PV technology. In addition, general rules of PV system installation must also be followed such as offset from the roof edge and row-to-row clearance within the PV system. Both restrictions can significantly reduce the roof coverage ratio of PV system which leads to a lower system DC yield.

To deliver a more realistic annual DC yield, a panel-fitting algorithm is first implemented on all building roof surfaces.^[15] This algorithm allows the population of PV modules onto roof surfaces with user-defined dimension and clearance in the intrinsic coordinate system. **Figure 12** schematically illustrates how the panel fitting with landscape configuration is implemented on a slanted roof. Since this algorithm works on the 2D plane, the roof surface is first projected to the ground and a rotation matrix M_R is applied to align the projected roof polygon with the intrinsic coordinate system. Depending on the roof orientation, this rotation can be clockwise or counter-clockwise to prevent the rotated polygon from being inverted. After that, an original bounding box is calculated for each roof polygon and a grid of PV modules is generated, considering the dimension of the selected PV module and the clearance as shown in Figure 12d.^[50] In the case of

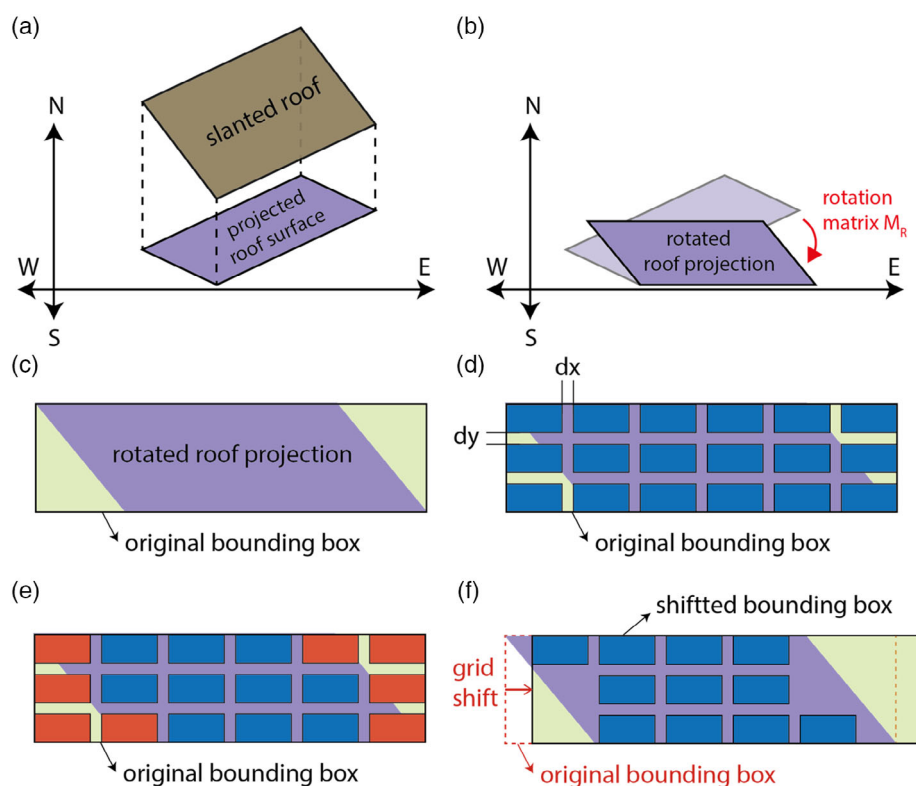


Figure 12. Schematic demonstration of panel fitting algorithm where a) roof surface is projected to the ground plane; b) rotate the roof with specific rotation matrix to be aligned with the intrinsic coordinate system; c) original bounding box is generated for the rotated roof projection; d) a grid of PV modules is generated with the selected PV module dimension and user-defined clearance; e) check which PV modules cannot be fitted on the roof where those colored in red are removed; and d) grid shift is applied to the entire grid of PV modules to find the optimal panel fitting result.

slanted roofs, no offset from the roof edge is considered and the clearance between PV modules is selected as 5 cm to allow the load and unload of modules for maintenance purposes. To determine which of the PV modules can be accommodated by the roof surface, the algorithm checks both if the four module corners are located within the roof polygon, and if the intersection between roof and module polygons is larger than 99%. Those who do not meet the conditions such as the modules colored in red in Figure 12e are removed from the result. The best panel fitting scenario is obtained by iterating through different grid shifts to maximize the number of fitted PV modules. In each iteration, the entire grid of modules is moved by a certain distance along x - and y -axes, respectively

$$\begin{cases} x_{shift} = -(L_M + G_x) \cdot \frac{i-1}{i} \\ y_{shift} = -(W_M + G_y) \cdot \frac{i-1}{i} \end{cases} \quad (2.3)$$

where L_M is the module length, W_M is the module width, G_x is the clearance along x axis, G_y is the clearance along y -axis, and i is the number of iteration. In portrait configuration, the module length and width in the equations are swapped. To reduce the computational burden, the iteration number is also adjusted based on the size of the roof. Large roofs with an area greater than 300 m² iterate 3 times, and small roofs with an area lower than 100 m² iterate 8 times. The rest undergo 5 iterations. Figure 12f shows the panel fitting result after grid shift. It turned out that one additional PV module is included compared to the original case. Finally, the fitted modules are repositioned with the transpose of rotation matrix M_R , and all the module corners are projected back to the roof plane so that the skyline can be correctly generated for both annual irradiation and DC yield calculation. This is done by finding the intersection between the line and plane as shown in Figure 13. The coordinates of intersection C can be calculated with variable t according to the following equation

$$\begin{cases} x = b_1 + v_1 \cdot t \\ y = b_2 + v_2 \cdot t \\ z = b_3 + v_3 \cdot t \end{cases} \quad (2.4)$$

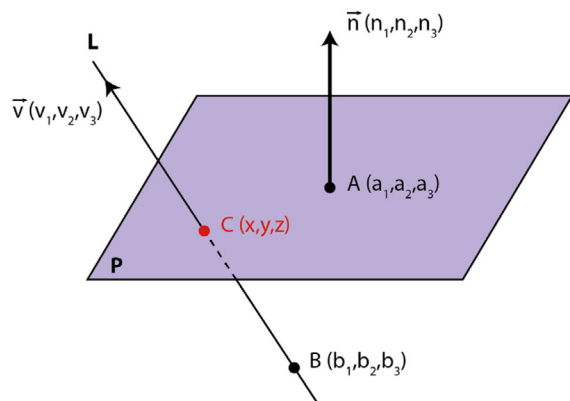


Figure 13. Schematic illustration of finding the intersection between the line and plane where A is a point on the plane, \vec{n} is the plane normal vector, B is an arbitrary point outside the plane which constructs line L with direction vector \vec{v} . Point C is the intersection between plane P and line L.

where

$$t = \frac{(a_1 - b_1) \cdot n_1 + (a_2 - b_2) \cdot n_2 + (a_3 - b_3) \cdot n_3}{n_1 \cdot v_1 + n_2 \cdot v_2 + n_3 \cdot v_3} \quad (2.5)$$

Point B is the coordinates of fitted PV module corner, vector \vec{v} is $[0,0,1]$, A is the coordinates of roof surface corner, and \vec{n} is the PV module face normal which is aligned with the roof surface normal in the case of slanted roofs.

Fitting panels onto flat roofs is more complicated. One challenge is not being able to use the roof surface normal to determine its orientation because the projection of face normal vector on the ground is 1D. This can be solved by using the directional vector of the longest roof edge as reference to represent roof orientation. Another challenge is to determine the tilt and orientation of PV modules because they cannot be inherited directly from the roof. Since the Netherlands is located in the northern hemisphere, PV systems on flat roofs ideally shall be oriented to the south such that the POA irradiation can be maximized. This is realized by segmenting the intrinsic coordinate system along the diagonals as illustrated in Figure 14a, and check to which segment does the roof orientation belong. If the roof orientation falls within the angle range segment A or C, the modules adopt this orientation. If the roof orientation is found in either angle range segment B or D, the module orientation is calculated to be perpendicular to the roof orientation. Additional angle shifts are applied to ensure that roof orientation always ends up in segment C to face south.

The last challenge is to define the correct rotation matrices to align the roof polygon with the intrinsic coordinate system. Since the coordinates of module polygon corners are arranged in a fixed order as shown in Figure 15a, the projected roof polygon shall be rotated in a way that it is aligned with the correct axis so that when the module polygons are projected back to the original flat roof surface, module corners 2 and 3 can be lifted off from the roof to correctly represent the module tilt geometrically. As an example, Figure 15c contains a projected flat roof polygon with the orientation $\vec{v}(v_1, v_2)$ defined by its longest edge. The rotation matrix M_R is applied so that the polygon is aligned with the X axis for panel fitting. As the fitted panels are projected back to the original flat roof surface, the module corners are wrongly lifted which results in an incorrect geometrical module tilt. To avoid such issue, different rotation matrices are introduced. Here, four-quadrant coordinate system is used for the ease of calculation. This coordinate system is geographically identical with the intrinsic one but uses an angle range $[-180^\circ, 180^\circ]$. It is divided into five segments as shown in Figure 14b, and for each segment, a specific rotation matrix is assigned according to Table 1 so that the roof polygon can be correctly rotated with the smallest angle to align with either X or Y axis for further panel fitting. Figure 15d shows the case where projected roof polygon is rotated to be parallel to the Y axis and a correct geometrical module tilt can be obtained. The module grid generation follows the standard PV system mounting configuration on flat roofs in the Netherlands where modules are tilted at 15° with a row-to-row spacing of 0.7 m.^[15] Apart from landscape and portrait configurations, dual-tilt configuration is also investigated where PV modules are tilted at 12° with a row-to-row clearance of 0.2 m.^[51] Its orientation is perpendicular to that of single-tilt

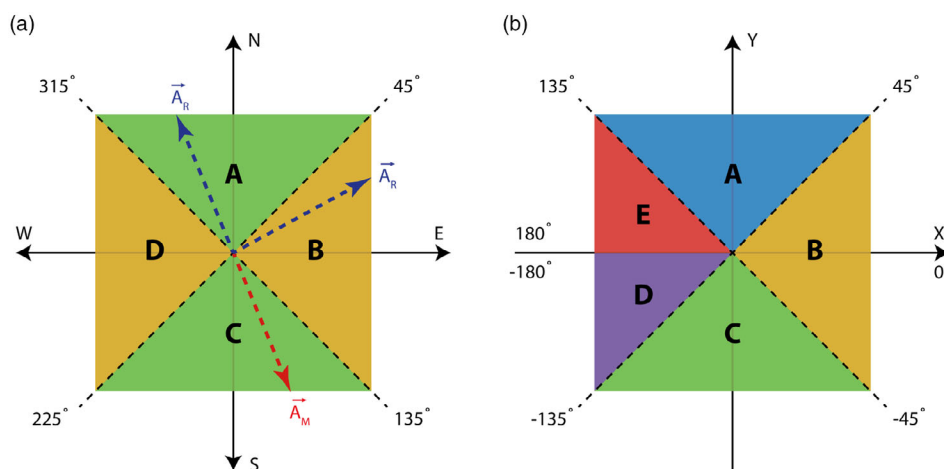


Figure 14. a) The intrinsic coordinate system where four angle range segments are defined. The module orientation \vec{A}_M is parallel to the roof orientation \vec{A}_R falling into segments A or C, and is perpendicular to the roof orientation \vec{A}_R falling into segments B or D; b) the coordinate system is divided into 5 sectors where each of them is assigned with a specific rotation matrix.

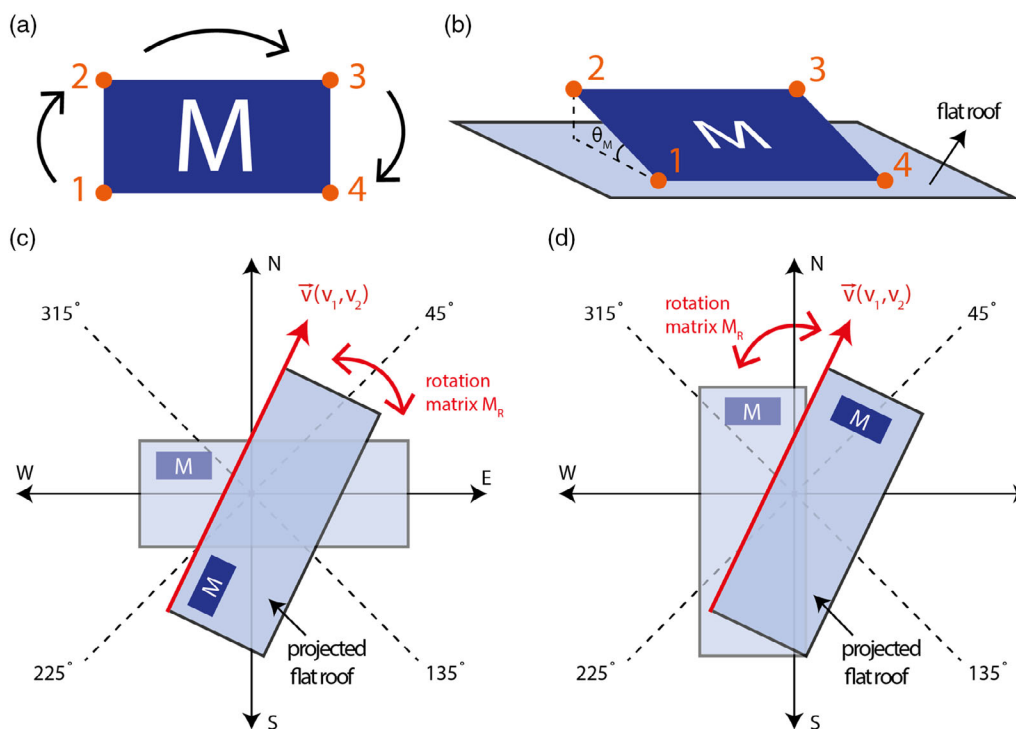


Figure 15. a) Module corners are saved in a fixed order which simplifies the process of geometrical module tilt creation; b) module corners 2 and 3 are lifted off from the flat roof with a defined tilt angle; c) rotated roof projection is aligned with the wrong axis which causes the incorrect geometrical module tilt representation; d) rotated roof projection is aligned with the proper axis which leads to a correct geometrical module tilt representation.

PV systems rather than being exactly east-west oriented because this ensures a larger packing density. Meanwhile, it is also reported that the dual-tilt configuration is not subject to power reduction when its orientation is off from east-west. In fact, it is benefiting from such angle deviation by producing slightly more energy.^[52] Additionally, flat-mounted PV system (with 0° tilt) was also studied for buildings with strict restrictions, such as monumental buildings and buildings locating at the streets

with protected view, to prevent the installed PV modules from being seen by the public at the street level.

Once the geographical coordinates of the fitted PV modules are obtained, points need to be uniformly generated on each module plane for annual DC yield calculation. The selected PV module has 72 solar cells in total, so ideally each solar cell shall be assigned with one point to maximize the result accuracy.^[50,51] But simulating 72 points per module exponentially

Table 1. Rotation matrices that assigned to the divided segments.

Segment	Rotation Matrix
A	$\begin{bmatrix} \cos(\frac{\pi}{2} - \alpha) & -\sin(\frac{\pi}{2} - \alpha) \\ \sin(\frac{\pi}{2} - \alpha) & \cos(\frac{\pi}{2} - \alpha) \end{bmatrix}$
B	$\begin{bmatrix} \cos(-\alpha) & -\sin(-\alpha) \\ \sin(-\alpha) & \cos(-\alpha) \end{bmatrix}$
C	$\begin{bmatrix} \cos(-\frac{\pi}{2} - \alpha) & -\sin(-\frac{\pi}{2} - \alpha) \\ \sin(-\frac{\pi}{2} - \alpha) & \cos(-\frac{\pi}{2} - \alpha) \end{bmatrix}$
D	$\begin{bmatrix} \cos(-\pi - \alpha) & -\sin(-\pi - \alpha) \\ \sin(-\pi - \alpha) & \cos(-\pi - \alpha) \end{bmatrix}$
E	$\begin{bmatrix} \cos(\pi - \alpha) & -\sin(\pi - \alpha) \\ \sin(\pi - \alpha) & \cos(\pi - \alpha) \end{bmatrix}$

increases the computational time, thus, it is decided to use a grid of 18 points on each module where every point represents a group of 4 solar cells. This balances the result accuracy and simulation time. Before proceeding with the DC yield mapping, there is one more issue needs to be tackled. As we have mentioned in Section 2.1, the reconstruction of 3D building models does not take into account the rooftop artifacts. This results in the overpopulation of PV modules on roofs as shown in **Figure 16a**. To exclude the PV modules that cannot be placed in real life due to the existence of rooftop obstacles, the annual solar irradiation is first calculated for each point of the module. If the minimum annual irradiation impinging on the module is lower than $600 \text{ kWh year}^{-1}$, it is removed. This irradiation limit also helps to exclude the PV modules that are subject to moderate shadings caused by the surrounding environment such as adjacent tall

buildings and giant vegetations. The DC yield of the remaining PV modules is calculated by using the simplified skyline-based model and the result is averaged over 18 points. Modules that deliver a specific yield smaller than 650 kWh kWp^{-1} are excluded due to economic feasibility.^[15] The final PV system topology is shown in **Figure 16b**, and it can be observed that the limits take out quite a few PV modules which are conflicting with the position of rooftop ventilation system.

Another issue with the current PV system configuration on flat roofs is the row-to-row mutual shading. To include the power reduction caused by mutual shading, the DSM is manipulated where points representing the fitted PV modules are added to the urban context. **Figure 17** compares the DSM of building 35 with/without the inclusion of module geometry. It is clear in **Figure 17c** that after DSM manipulation, the original roof surface points are replaced by the module points. Such environmental feature update is incorporated in the skyline profile generation which leads to a different set of SVF and SCF for DC yield calculation. Meanwhile, particularly for portrait configuration, the DC yield for each module is determined by the annual energy output of the bottom cell string due to the bypass diode effect.^[53] This effect is not included in the landscape configuration because it is more resilient to mutual shading based on the way solar cells are connected to the bypass diodes in conventional PV modules.^[54]

The DC yield for facades is mapped without panel fitting due to the shortage of digital façade information such as location of windows. Therefore, the façade DC yield map is generated based on surface points, like that of the annual solar irradiation map while the value of the surface points is replaced by annual DC yield. To extract out the numeric result for facades, we used

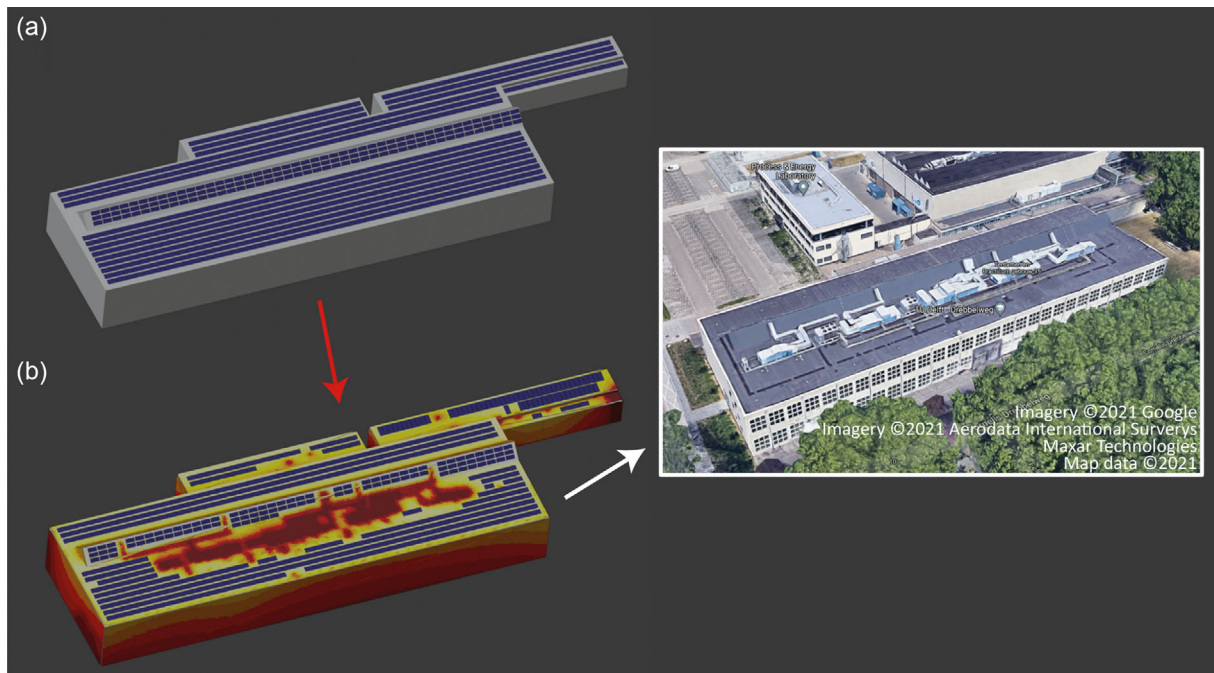


Figure 16. Panel fitting results of Building 35 of TU Delft campus where a) rooftop is fully populated with PV modules considering the module dimension and mounting configuration; b) modules whose minimum received irradiation and specific yield is lower than $600 \text{ kWh year}^{-1}$ and 650 kWh kWp^{-1} , respectively, are removed. The aerial photo is obtained from GoogleMap.

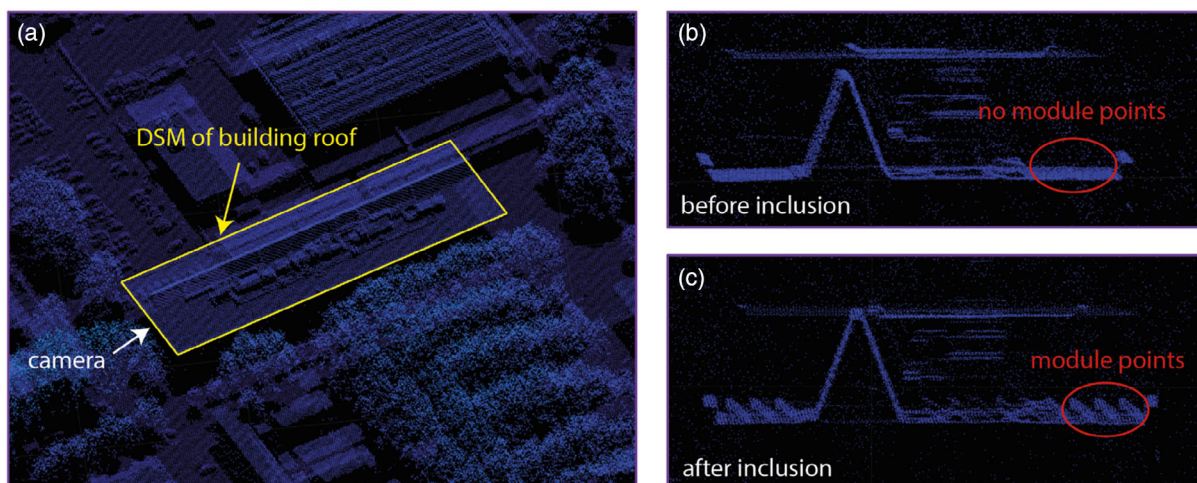


Figure 17. Manipulation of urban environment a) DSM of building roof where camera indicates the perspective of subfigures b and c generation; b) original roof plane DSM where no modules points are found; c) manipulated roof plane DSM where fitted module points are added to the urban context.

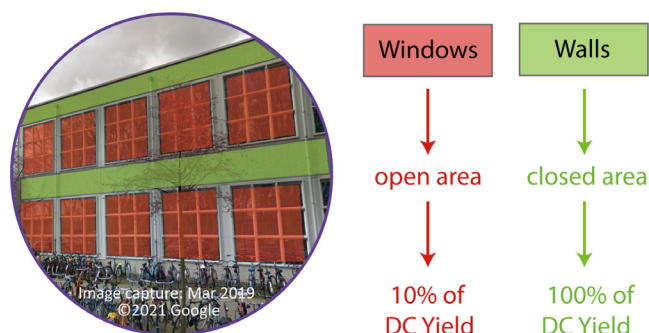


Figure 18. Facade DC yield mapping where windows (indicated in red polygons) are delivering 10% power of the classic PV modules; walls (indicated in green polygons) are delivering full power.

open/closed ratio which is calculated from GoogleMap StreetView images by estimating the area of windows and walls through visual inspection as shown in **Figure 18**. Windows, indicated by the red polygons, are classified as open surfaces. They are the good candidates for transparent PVs and it is assumed to deliver 10% power of the selected PV module. Walls as indicated by the green polygons, are classified as closed surfaces. Their DC yield is determined by multiplying the closed ratio with the total façade DC yield which is calculated over all the surface points. The economic threshold is not applied in this case otherwise only limited number of façade surfaces can be filtered in.

2.4. Annual AC Yield Mapping

Energy yield on the AC side is calculated by considering a chain of system losses. Among others, the inverter conversion efficiency is determined by using the SNL model,^[55] where 4 inverters with different nominal AC output power are chosen (1.5,^[56] 3,^[57] 6,^[58] and 12 kW^[59]). Each of them can accommodate 5, 10, 20, and 40 selected PV modules, respectively, considering a DC-AC performance ratio of 1.2.^[60] The type and number of inverters

assigned to each rooftop PV system is estimated based on the maximum number of PV modules in the system which is obtained from the panel fitting result. The workflow of inverter selection is schematically shown in **Figure 19**. To calculate the inversion efficiency, first a set of inverter efficiency curves are generated with the SNL model coefficients of each individual inverter. By locating the ratio of annual DC yield of the PV system and the estimated annual P_{dc0} of the inverters on the curve, the conversion efficiency for each specific PV system is determined. Here, the inverters are assumed to be working for half year of 4380 h. Additional fixed conversion efficiencies for MPPT (98%), ohmic loss (99%), module mismatch (99%), and soiling loss (98%) are considered to calculate the overall DC-AC conversion efficiency.^[61] As for the facades, since no panel fitting is implemented, a fixed DC-AC conversion efficiency of 91% is assumed.

2.5. Roof Segments Classification

Finally, the roof segments are classified based on the specific yield of the PV system mounted. Three categories are considered, and each category is assigned with an individual color: red ($650 \approx 800 \text{ kWh kWp}^{-1}$), yellow ($800 \approx 950 \text{ kWh kWp}^{-1}$), and green ($>950 \text{ kWh kWp}^{-1}$). The outcome of each step of the workflow is shown in **Figure 20** for Building 35 on TU Delft campus. The AC yield map is in overall darker than the DC yield map due to the system losses, and the map of roof classes provides an indication on which roof surface shall be prioritized for PV integration.

3. Results and Discussion

In this section, the numerical results of solar PV scan on TU Delft campus are discussed. Again, Building 35 is used as an example and an overall analysis on the campus scale will be made later on. The entire study is based on Solarge SOLO and Solarge

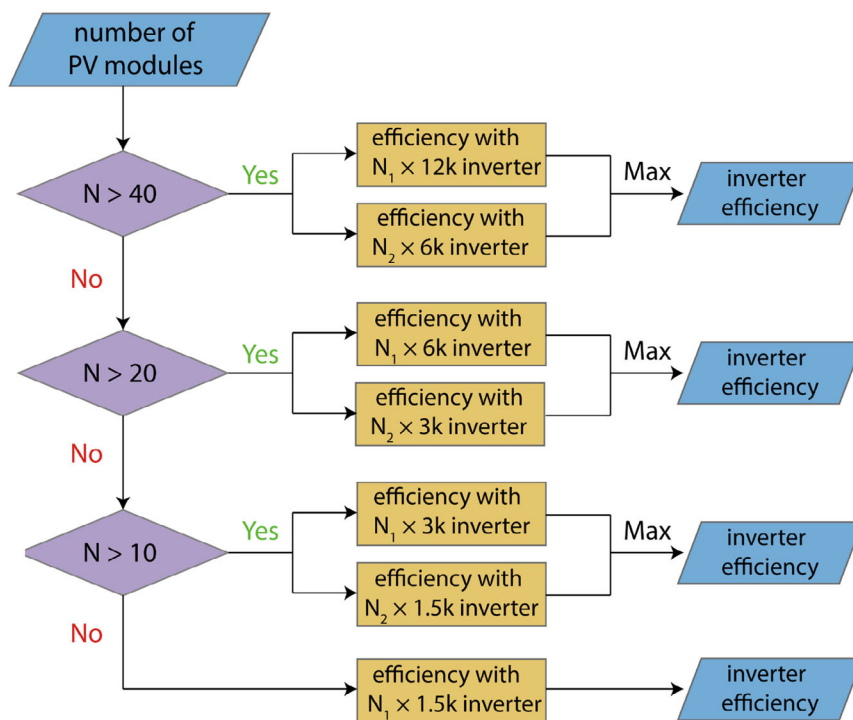


Figure 19. Workflow of determining the type and number of inverters used to estimate the inversion efficiency of rooftop PV system where N_1 and N_2 indicate the number of inverters.

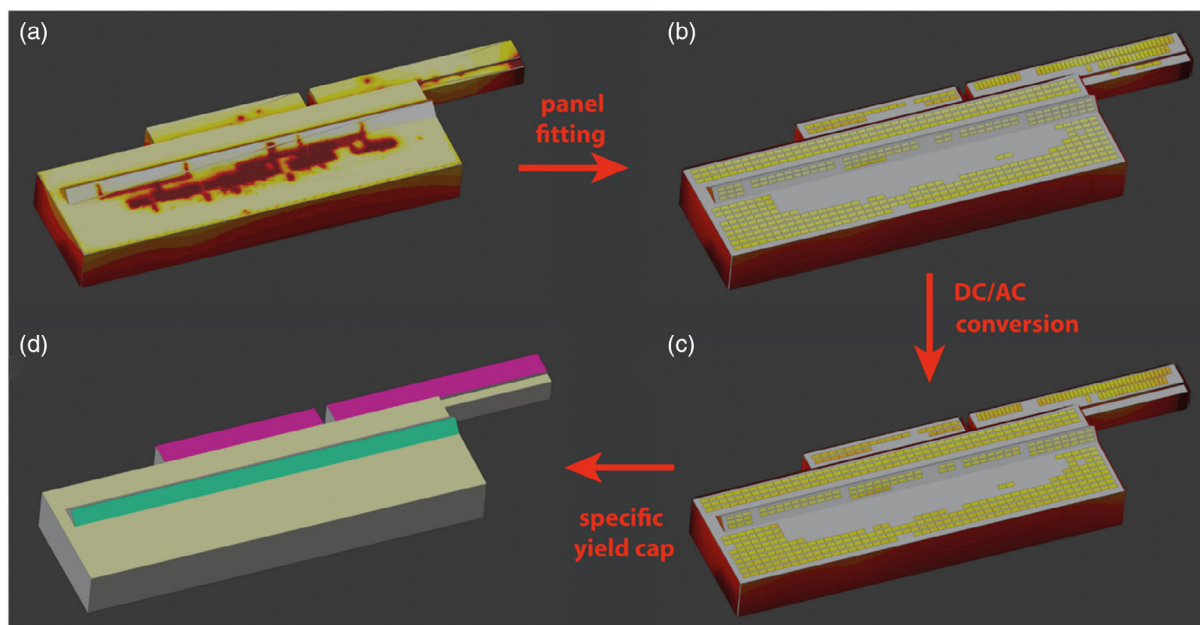


Figure 20. Annual a) solar irradiation map; b) DC yield map; c) AC yield map; and d) roof classes of Building 35 on TU Delft campus.

DUWO solar modules.^[50,51] Both of them deliver the same peak power of 365 Wp. The dimension of these two types of module is slightly different where Solarge SOLO is reported to be 2.066×0.997 m while Solarge DUWO is 2.021×0.997 m with a default tilt of 12° .

3.1. Computational Speed

The simulation time for Building 35 in each step is listed in **Table 2** where the mapping of DC/AC yield is the most time-consuming process, followed by the annual solar irradiation

Table 2. Breakdown of the simulation time of building 35 on TU delft campus.

Building number and name	Building 35 (Drebbelweg)
Barycentric coordinate system [s]	0.3
Generation of solar irradiation map [s]	172
Panel fitting on roofs [s]	76
Generation of DC & AC yield maps [s]	276
Roof segment classification [s]	0.1
Total simulation time [s]	524 [s] = 8.7 [min]

mapping. This is because prior to the generation of DC/AC yield maps, an additional step of solar irradiation calculation is carried out for each point on the PoA to exclude the modules that are subject to considerable shading due to the conflict with the position of rooftop obstacles or to the surrounding environment. Meanwhile, DC/AC yield mapping is done on a grid of 18 points per module, indicating that each point represents an area of roughly 0.1 m^2 . Compared to that for solar irradiation map (0.25 m^2), the point density is doubled, and a longer computational time can be expected. One approach to reduce the computational time for DC/AC yield map generation would be simultaneously calculating the module DC/AC yield during the exclusion of shaded modules. Currently these two processes are done separately which requires double calling of HorizonScanner function to generate the skyline. Another alternative approach that might drastically reduce the computational time of this part would base on machine-learning or look-up tables where the results from the annual solar irradiation map can be utilized as primary values to look up the secondary values for DC/AC yield.

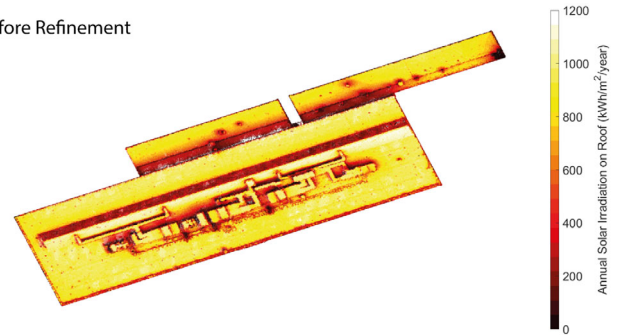
The computational speed per step is averaged over all TU Delft buildings and the results are listed in **Table 3**. The overall computational speed is found at 0.085 s m^{-2} with a standard deviation (SD) of 0.044 s m^{-2} . Panel fitting shows relatively the highest SD because the iteration of grid shift depends on the size of the roof. Roofs with an area larger than 300 m^2 iterate 3 times while those with an area smaller than 100 m^2 iterate 8 times. The rest roofs undergo 5 iterations. Therefore, for buildings with large amount of small roofs, the speed is lowered due to more iterations.

Figure 21 compares the annual solar irradiation maps generated before and after building model refinement. One of the drawbacks of using unrefined model for solar potential

Table 3. Computational speed per step for solar PV potential map generation in MATLAB.

	Averaged Speed [s m^{-2}]	Standard Deviation [s m^{-2}]
Barycentric coordinate system	5.67E-05	3.89E-05
Generation of solar irradiation map	0.016	0.006
Panel fitting on roofs	0.015	0.011
Generation of DC & AC yield maps	0.054	0.027
Overall computational speed	0.085	0.044

Before Refinement



After Refinement

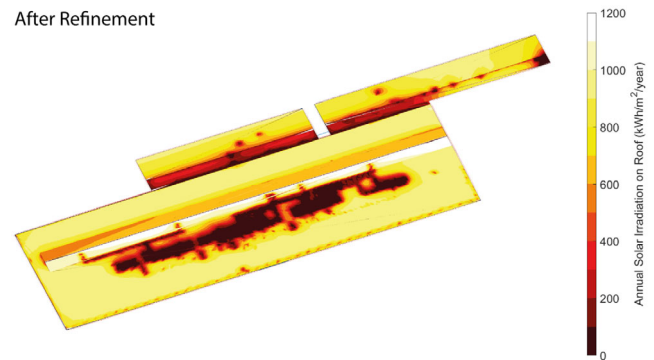


Figure 21. Annual solar irradiation maps for building 55 before and after 3D building model refinement.

calculation is that the discrepancy in tilt and orientation between adjacent triangles can lead to very different results. This creates unexpected dark spots which scatter over the entire roof surface as it is shown in the figure. In addition, the solar irradiation calculation is also performed for rooftop obstacles in unrefined case. This is evident from the high irradiation value at the region where obstacles sit, which can overestimate the geographical potential. In terms of computational speed, the unrefined model takes 37 min to generate the surface points (by finding the center point of each triangular mesh) and perform the solar irradiation mapping, while using refined model is 13 times faster as compared in **Table 4**. For unrefined model, the roof surface area is calculated by summing up the area of all roof triangular meshes. The result is about 8% larger than the refined case, and this can be mainly attributed to the misalignment between triangular meshes. This result will be more accurate if the projection area of the triangular meshes is used for calculation. The total roof annual irradiation for both cases is very close where unrefined model reports a roughly 3% higher result. Such increase, as

Table 4. Comparison of computational speed and simulation results of building 55 before and after 3D building model refinement.

	Unrefined Model	Refined Model
Surface points generation [s]	79.9	0.31
Generation of solar irradiation map [s]	2149.9	172.1
Roof surface area [m^2]	4417	4075
Total roof annual irradiation [GWh year^{-1}]	3.03	2.95

mentioned previously, is partially due to the inclusion of irradiation results of rooftop obstacles. Misalignment between triangular meshes can also cause this deviation but it might cancel out at a roof plane scale.

3.2. Solar PV Potential Mapping on TU Delft Campus

Table 5 lists the simulation results of Building 35 where two building surfaces are presented in detail as shown in Figure 22. This building is unrestricted, so three mounting configurations are investigated for flat roof surface. From the table we can conclude that for roof 1, dual-tilt configuration allows the maximum population of PV modules. This is because the reduction in row-to-row clearance significantly increases the packing density. Meanwhile, it can be seen that landscape configuration has the highest specific yield while the portrait configuration delivers the lowest. This is mainly due to the mutual shading occurred between rows which drastically bring down the power output of modules in portrait configuration. The highest system DC/AC yield is produced in dual-tilt configuration because of its largest system size, even though its specific yield is not the best. In fact, dual-tilt is found to be the optimal mounting configuration for the majority of flat roofs in this study in terms of energy output. It makes sense to trade for higher packing density with some small sacrifice in power productivity of each individual module. As for roof 2, both landscape and portrait configurations have similar specific yield where the higher hits around $1014 \text{ kWh kWp}^{-1}$. It is more favorable than that on roof 1 because of a more optimal module tilt (41°) which is inherited directly from the roof. In contrast, the façade is delivering much lower energy yield with a unit AC yield of $26 \text{ kWh m}^{-2} \text{ year}^{-1}$. This low performance can be attributed to 1) vertical façades generally have lower SVF which limits the amount of incident irradiance; 2) high density of towering trees at the front cause extensive shadings on the façade as can be seen in Figure 16.

The same simulation has been done on all the buildings of TU Delft campus. It turned out that a total of $8.1 \text{ GWh year}^{-1}$ PV potential can be harvested, where roofs contribute around $4.7 \text{ GWh year}^{-1}$ and the rest $3.4 \text{ GWh year}^{-1}$ is covered by façades. As there is no panel fitting done for the façades, the same economic threshold of 650 kWh kWp^{-1} is translated to 113 kWh m^{-2} considering the peak power and dimension of selected module. The analysis shows that only two façades throughout the campus reach this limit, and their annual AC

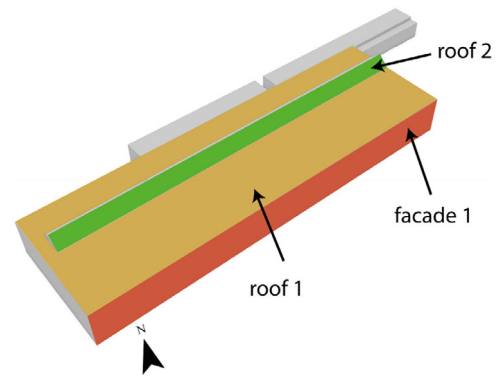


Figure 22. 3D model of Building 35 on TU Delft campus where the simulation results of flat roof (colored in yellow), slanted roof (colored in green), and facade (colored in red) are presented.

yield totals $118.2 \text{ MWh year}^{-1}$ which accounts for only 3.5% of the case without filter. Applying the same economic threshold to the façades, we will end up with lower total annual AC yield of $4.8 \text{ GWh year}^{-1}$ which demonstrates roof surfaces as low-hanging fruits for PV integration on campus. To visualize the results, a *high resolution 3D solar PV potential map* has been published as a web scene where a screen shot of the annual solar irradiation map can be found in Figure 23. This web map can be accessed with personal Google account, and it contains the visualization of all simulation results including 3D building models, the annual solar irradiation map, panel fitting results on the roofs, DC yield map, AC yield map and roof classes. The detailed modeling method applied to roofs indicates that rooftop solar PV potential has a high level of confidence, whereas façades have a relatively low level of confidence due to the shortage of digital façade information. Therefore, the technical potential on façades is most likely overestimated because surfaces that are not suitable for module installation in practice (such as narrow walls between windows) are still taken into account in the calculation.

The total electricity demand on the entire campus is $82.6 \text{ GWh year}^{-1}$,^[62] meaning that roughly 10% of the current electricity demand can be supplied by roof and façade PVs based on this study. It is worth noting that this calculation simply divides the simulated PV energy by the current electricity demand on campus, in other words, it assumes all PV generation is self-consumed by the building. Meanwhile, all PV systems are

Table 5. Simulation results of building 35 on TU delft campus where building surfaces are analyzed in detail.

	Mounting Configuration [-]	Number of Modules [-]	Specific Yield [kWh kWp^{-1}]	DC Yield [MWh]	AC Yield [MWh]
Roof 1 (flat)	Landscape	376	921.9	126.5	116.3
	Portrait	442	772.3	124.6	114.3
	Dual-tilt	549	835.5	167.4	153.7
Roof 2 (slanted)	Landscape	94	1003.9	34.4	31.7
	Portrait	80	1013.9	29.6	27.2
	Area [m^2]	Open Ratio [%]	Closed Ratio [%]	DC Yield [MWh]	AC Yield [MWh]
Façade 1	1104.4	55	45	32.1	29.0

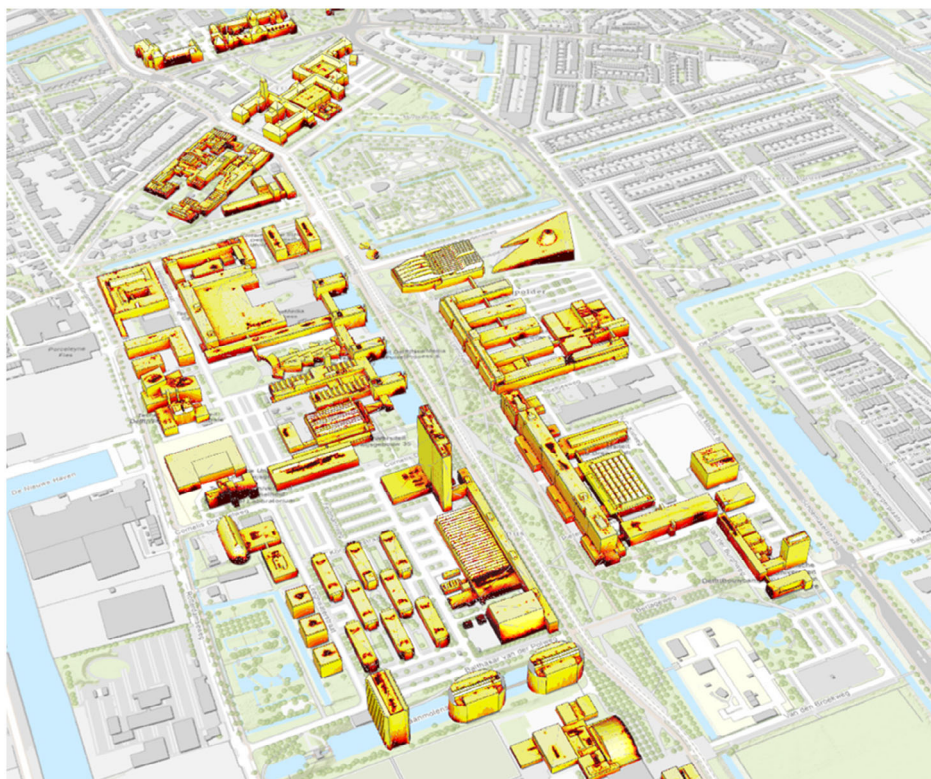


Figure 23. Annual solar irradiation map for TU Delft campus. Through this link <https://tudelft.maps.arcgis.com/home/webscene/viewer.html?webscene=0bc9d9485c334a07aa05402238776477>, one can see all the simulation results by logging in with a personal Google account.

connected to the grid. The grid is acting as a big battery and the losses in the round trip of injecting electricity to or getting it back from the grid are neglected. Here, a grid parity is also assumed where the levelized cost of electricity (LCoE) is lower than or equal to the price of purchasing electricity from the grid. However, this share is still quite off from the goal that 50% of the electricity consumption shall be covered by renewable energy sources by 2030. Continuous studies need to be conducted to improve the PV penetration, such as extending the solar PV mapping to open areas and waterways and using PV modules with higher efficiency for simulation. In addition, the to-be-constructed buildings on TU Delft campus south also serve as good candidates for PV integration. Assuming the newly constructed buildings are more energy efficient and demanding less electricity, adding PV to them will increase the current 10% share.

4. Validation Study

The PV system installed on the low-rise of EWI faculty building is studied to validate the simulation results from our workflow. Currently, there are 521 mounted PV modules whose locations are shown in the GoogleMap image in **Figure 24**. Based on the data provided by Campus Real Estate (CRE), this system has a total capacity of 133.56 kWp, indicating that the peak power of each PV module is 255 Wp. The final panel fitting result for the same rooftops is also presented in Figure 24 where 1064

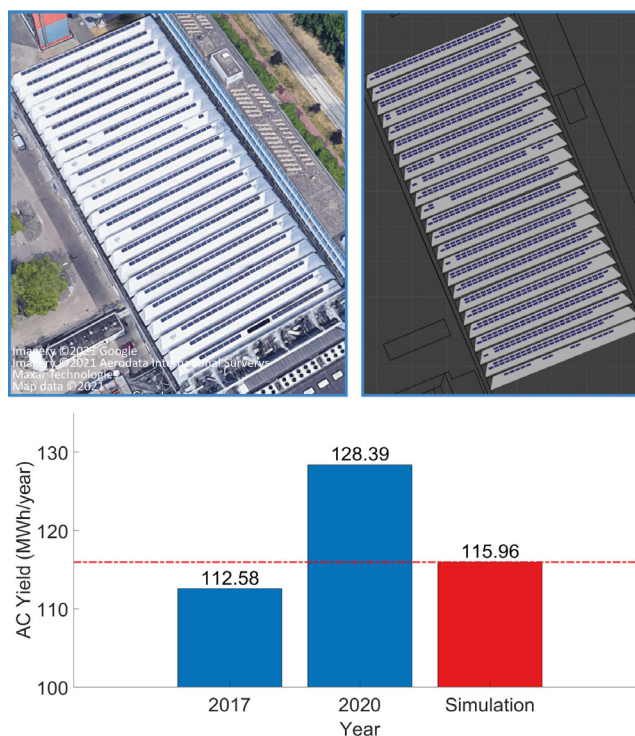


Figure 24. Validation of simulation results where the PV system installed on rooftops of EWI low-rise building is studied.

PV modules are reported. The number of modules is almost doubled because our algorithm tries to accommodate as many PV modules as possible on the roof as long as the economic threshold is not violated. Given such system layout, our simulation reports an annual AC yield of $236.82 \text{ MWh year}^{-1}$ which is further corrected to $115.96 \text{ MWh year}^{-1}$ by considering the module number correction factor of 0.4896. Compared to the real system output data in 2017 ($112.58 \text{ MWh year}^{-1}$) and 2020 ($128.39 \text{ MWh year}^{-1}$) shared by the operator, our simulation falls within the energy variation range and shows a high level of fidelity.

5. Limitations and Outlook

During the course of this study, several limitations have been identified. The first limitation has to do with the accuracy of the input dataset. As it is discussed in Section 2.1, the current LiDAR data of TU Delft campus was collected in 2014. Therefore, any construction changes or environmental development happened after 2014 is not included. This outdated input can cause quite some deviation in the result if there has been some fast growth of vegetation or huge renovation on campus building roofs where previously available surfaces are no longer useable for PV installation due to newly added artifacts. The density of AHN3 is about $3\text{--}5 \text{ points m}^{-2}$ where more than 99.7% of the points have an accuracy of 20 cm.^[39] This makes it hard to detect small and low rooftop obstacles such as roof lights. The good news is that a new set of LiDAR data for the entire Netherlands has been collected (AHN4) and will be published soon. This new LiDAR dataset has on average $10\text{--}14 \text{ points m}^{-2}$ which allows the generation of DSM with higher resolution. With a more detailed urban environment representation, a higher accuracy of the results from this workflow can be expected.

The second limitation comes from the modeling of trees. Current algorithm assumes them to be opaque due to the nature of AHN3 dataset, but in real life, light can still find its path through the foliage. Particularly in winter when there is barely any leaves on trees, the chance of light reaching the PV module surface is increased and a higher power output can be expected. The third category that requires special attention is the curving slopes of buildings because they are constructed from polygonal surfaces. Therefore, a continuous curvature does not exist but instead it is replaced by multiple polygons of individual normal vector. Increasing the number of polygons can better reproduce the curving slope but at the meantime, if the polygon size is too small to fit PV modules, then no panel fitting result will come out. Meanwhile, the reconstruction of 3D building models still remains semiautomatic, and to the authors' knowledge, there are some groups working on automatic 3D building model reconstruction from LiDAR data.^[63–65] A collaboration can be expected to realize a fully automatic PV AC yield modeling framework based on LiDAR data and building footprint.

The integrability of PV in building envelop is not considered in this work. For example, current analysis does not include the roof load capacity which might lead to an overestimation of roof PV potential. The social impact of PV integration in buildings, such as visibility and aesthetic of PV systems, also requires

additional research to deliver a more realistic potential to decision makers. Such impact is less significant to roofs (particularly flat ones) as they are less visible to the public domain, while facades are more visible to the urban dweller, the aesthetic aspect shall be taken into account. Future research can be made on visibility assessment of building surfaces to the public domain which helps PV engineers to identify the low-hanging fruits where PV systems are barely visible. Colored PV can be used to solve the aesthetic issue of visible surfaces. Their performance in terms of power reduction can be modelled and integrated into the current workflow. Such modelling frameworks can be further adjusted when the PV community is more mature in producing commercial colored PV modules.

6. Conclusion

In this work, we presented an innovative workflow to assess the solar PV potential in a large urban area where TU Delft campus is taken as the case study. This workflow starts with the reconstruction of 3D building models in a semiautomatic method. Here, LiDAR data and building footprints are used to reconstruct original building models in ArcGIS Pro which are later polished in Blender. These highly accurate 3D building models are loaded into MATLAB, and barycentric coordinate system is implemented to generate a uniformly distributed grid (0.5 m) on building surfaces. After that, the annual solar irradiation for each surface point is calculated by using our in house developed simplified skyline-based model.

In addition to investigating the physical potential, this approach also studied the technical potential and economic potential. This is done by first populating each roof segment with selected PV module dimension and defined clearance. A grid shift is applied to find the maximum panel fitting scenario. Then the same simplified skyline-based model is used to calculate annual POA solar irradiation and DC yield. In this case, a grid of 18 points per module is used to balance the result accuracy and computational burden. To exclude the modules whose position is occupied by roof obstacles, the algorithm checks if the minimum annual solar irradiation received by the module is lower than $600 \text{ kWh m}^{-2} \text{ year}^{-1}$. Meanwhile, if the specific yield of PV module is lower than 650 kWh kWp^{-1} , it is also removed from the result due to economic feasibility. Particularly in the case of flat roofs, three mounting configurations are investigated: landscape, portrait, and dual-tilt. Such calculation also considers the yield reduction due to row-to-row mutual shading and bypass diode effect. On the AC side, the SNL model is used to estimate the inverter efficiency for rooftop PV systems.

The DC and AC yield calculation for facades are approached in a different way since no digital façade information is available. Therefore, open/closed ratio estimated from Google StreetView images is used to determine the façade DC yield, and it is assumed that closed surfaces (walls) are delivering 100% of calculated DC yield while open surfaces (windows) are producing 10% of calculated DC yield. Finally, roof segments are classified into three categories based on the specific yield of the mounted PV system. The final solar PV potential maps are published in ArcGIS web scene and can be accessed by using personal Google account.

The simulation result shows that a total of 8.1 GWh year⁻¹ PV potential can be harvested from campus building roofs and facades. As the study demonstrates, our contributed modeling framework paves the way for a quick and accurate assessment of PV potential (from physical potential to economic potential) on a large-scale and complex urban environment.

Acknowledgements

The authors would like to acknowledge CRE for the funding, the Dutch government for providing the freely available LiDAR data and GIS data, and FME workbench for providing free academic license which has been extensively used for data format transform. The authors are also grateful for the façade open/closed ratio data provided by Michiel Fremouw and Puji Nata Djaja.

Conflict of Interest

The authors declare no conflict of interest.

Data Availability Statement

Research data are not shared.

Keywords

building integrated PV, complex geometry, electrical energy yield simulation, modeling, photovoltaic potential, solar mapping, urban PV

Received: June 30, 2021

Revised: October 17, 2021

Published online:

- [1] *The Paris Agreement | UNFCCC - Preview of Related Info | Mendeley*, https://www.mendeley.com/catalogue/89fa82a2-0626-3e2b-aff2-65b544022a7d/?utm_source=desktop&utm_medium=1.19.8&utm_campaign=open_catalog&userDocumentId=%7B048743f8-df04-3261-acc5-5e19e6e30012%7D.
- [2] *Climate policy | Climate Change | Government.nl*, <https://www.government.nl/topics/climate-change/climate-policy>.
- [3] D. E. Van Den Biggelaar, *Master Thesis, Delft University of Technology* **2018**.
- [4] *Lost in Transmission: How Much Electricity Disappears Between a Power Plant and your Plug? | Inside Energy*, <http://insideenergy.org/2015/11/06/lost-in-transmission-how-much-electricity-disappears-between-a-power-plant-and-your-plug/> (accessed: October 2021).
- [5] B. Cohen, *Cornerstone* **2015**, 3, 4.
- [6] *How can we Make the Campus Climate-Neutral in 10 Years?* <https://www.delta.tudelft.nl/article/how-can-we-make-campus-climate-neutral-10-years> (accessed: October 2021).
- [7] B. Norton, P. C. Eames, T. K. Mallick, M. J. Huang, S. J. McCormack, J. D. Mondol, Y. G. Yohanis, *Sol. Energy* **2011**, 85, 1629.
- [8] C. Ferri, H. Ziar, T. T. Nguyen, H. van Lint, M. Zeman, O. Isabella, *Renewable Energy* **2022**, 182, 427.
- [9] H. Ziar, B. Prudon, F. Y. Lin, B. Roeffen, D. Heijkoop, T. Stark, S. Teurlincx, L. de Senerpont Domis, E. G. Goma, J. G. Extebarria, I. N. Alavez, D. van Tilborg, H. van Laar, R. Santbergen, O. Isabella, *Prog. Photovolt. Res. Appl.* **2021**, 29, 725.
- [10] S. Jige Quan, Q. Li, G. Augenbroe, J. Brown, P. Pei-Ju Yang, P. Pei-Ju Yang, *Energy Procedia* **2015**, 75, 2946.
- [11] *Solar cells on TU Delft roofs—Campus Development—TU Delft*, <https://campusdevelopment.tudelft.nl/en/project/solar-cells-on-tu-delft-roofs/> (accessed: October 2021).
- [12] H. Ziar, P. Manganiello, O. Isabella, M. Zeman, *Energy Environ. Sci.* **2021**, 14, 106.
- [13] S. Kucuksari, A. M. Khaleghi, M. Hamidi, Y. Zhang, F. Szidarovszky, G. Bayraksan, Y. J. Son, *Appl. Energy* **2014**, 113, 1601.
- [14] K. Mainzer, S. Killinger, R. McKenna, W. Fichtner, *Sol. Energy* **2017**, 155, 561.
- [15] T. N. C. de Vries, J. Bronkhorst, M. Vermeer, J. C. B. Donker, S. A. Briels, H. Ziar, M. Zeman, O. Isabella, *Sol. Energy* **2020**, 209, 96.
- [16] J. E. Fuentes, F. D. Moya, O. D. Montoya, *Electronics* **2020**, 9, 2144.
- [17] M. Vermeer, *Master Thesis, Delft University of Technology*, **2018**.
- [18] R. (O. C.) Tse, C. Gold, D. Kidner, in *Advances in 3D Geoinformation Systems*, Springer, Berlin, Heidelberg **2008**, pp. 161–175.
- [19] *What is Lidar Data?—Help | ArcGIS Desktop*, <https://desktop.arcgis.com/en/arcmap/10.3/manage-data/las-dataset/what-is-lidar-data.htm> (accessed: October 2021).
- [20] *What Is Spatial Data? The Basics & GIS Examples | FME*, <https://www.safe.com/what-is/spatial-data/> (accessed: October 2021).
- [21] S. Izquierdo, M. Rodrigues, N. Fueyo, *Sol. Energy* **2008**, 82, 929.
- [22] L. Bergamasco, P. Asinari, *Sol. Energy* **2011**, 85, 1041.
- [23] M. C. Brito, N. Gomes, T. Santos, J. A. Tenedório, *Sol. Energy* **2012**, 86, 283.
- [24] J. B. Kodysh, O. A. Omiaomu, B. L. Bhaduri, B. S. Neish, *Sustain. Cities Soc.* **2013**, 8, 31.
- [25] F. Mansouri Kouhestani, J. Byrne, D. Johnson, L. Spencer, P. Hazendonk, B. Brown, *Int. J. Energy Environ. Eng.* **2019**, 10, 13.
- [26] M. C. Brito, P. Redweik, C. Catita, S. Freitas, M. Santos, *Energies* **2019**, 12, 3457.
- [27] J. Hofierka, J. Kaňuk, *Renew. Energy* **2009**, 34, 2206.
- [28] T. Santos, N. Gomes, S. Freire, M. C. Brito, L. Santos, J. A. Tenedório, *Appl. Geogr.* **2014**, 51, 48.
- [29] C. Catita, P. Redweik, J. Pereira, M. C. Brito, *Comput. Geosci.* **2014**, 66, 1.
- [30] A. Vulkan, I. Kloog, M. Dorman, E. Erell, *Energy Build.* **2018**, 169, 97.
- [31] A. V. Vo, D. F. Laefer, A. Smolic, S. M. I. Zolanvari, *ISPRS J. Photogramm. Remote Sens.* **2019**, 155, 119.
- [32] S. M. Murshed, A. Lindsay, S. Picard, A. Simons, in *The Annual International Conference on Geographic Information Science*, Springer, Cham, June **2018**, pp. 27–53.
- [33] M. Amado, F. Poggi, *Energy Procedia* **2014**, 48, 1539.
- [34] T. Ramkumar, H. Gamage, E. W. Xiao, M. Cassat, *J. Phys.: Conf. Ser.* **2019**, 1343, 012050.
- [35] S. Freitas, C. Catita, P. Redweik, M. C. Brito, *Renew. Sustain. Energy Rev.* **2015**, 41, 915.
- [36] A. Calcabrini, H. Ziar, O. Isabella, M. Zeman, *Nat. Energy* **2019**, 4, 206.
- [37] A. M. Martín, J. Domínguez, J. Amador, *AIMS Energy* **2015**, 3, 326.
- [38] *The Basics of LiDAR - Light Detection and Ranging - Remote Sensing | NSF NEON | Open Data to Understand our Ecosystems*, <https://www.neonscience.org/resources/learning-hub/tutorials/lidar-basics> (accessed: October 2021).
- [39] *Quality description | AHN*, <https://www.ahn.nl/kwaliteitsbeschrijving> (accessed: October 2021).
- [40] *Compare Analysis*, <https://hwh.maps.arcgis.com/apps/CompareAnalysis/index.html?appid=b2d67e3a99cf47759d34b19476476889> (accessed: October 2021).
- [41] *Datasets - PDOK*, <https://www.pdok.nl/datasets> (accessed: October 2021).

- [42] *LAS Building Multipatch (3D Analyst)—ArcGIS Pro | Documentation*, <https://pro.arcgis.com/en/pro-app/latest/tool-reference/3d-analyst/las-building-multipatch.htm> (accessed: October 2021).
- [43] *Decimate Modifier — Blender Manual*, <https://docs.blender.org/manual/en/latest/modeling/modifiers/generate/decimate.html> (accessed: October 2021).
- [44] P. Manganiello, M. Baka, H. Goverde, T. Borgers, J. Govaerts, A. van der Heide, E. Voroshazi, F. Catthoor, in *2017 IEEE 44th Photovoltaic Specialist Conf. (PVSC)*, IEEE, June **2017**, p. 3343–3347.
- [45] F. Catthoor, M. Baka, P. Manganiello (IMEC VZW), *US 10963603 B2*, **2021**.
- [46] *Topographic Mapping - Above Surveying*, <https://www.abovesurveying.com/inspection/topographic-mapping/> (accessed: October 2021).
- [47] P. B. Laval, *Mathematics for Computer Graphics-Barycentric Coordinates*, Kennesaw State University, Tech. Rep. **2003**.
- [48] *Ray Tracing: Rendering a Triangle (Barycentric Coordinates)*, <https://www.scratchapixel.com/lessons/3d-basic-rendering/ray-tracing-rendering-a-triangle/barycentric-coordinates> (accessed: October 2021).
- [49] M. C. Keijzer, *Master Thesis, Delft University of Technology* **2019**.
- [50] *Solarge SOLO*, <https://solarge.com/producten/solarge-solo> (accessed: October 2021).
- [51] *Solarge DUO*, <https://solarge.com/producten/solarge-duo> (accessed: October 2021).
- [52] *What happens when an east-west solar array isn't perfectly east-west?* <https://www.solarpowerworldonline.com/2016/10/happens-east-west-solar-array-isnt-perfectly-east-west/> (accessed: October 2021).
- [53] S. Silvestre, A. Boronat, A. Chouder, *Appl. Energy* **2009**, 86, 1632.
- [54] *Technical Note Bypass Diode Effects in Shaded Conditions*, SolarEdge CO. Ltd., technical report, available on [October 2021], https://www.solaredge.com/sites/default/files/se_technical_bypass_diode_effect_in_shading.pdf.
- [55] *PV LIB Matlab Help*, https://pvpmc.sandia.gov/PVLIB_Matlab_Help/ (accessed: October 2021).
- [56] *Blueplanet 02xi and 02x Grid-Tied Inverter, datasheet, KACO String Inverter Technology*, available on [October 2021]. <https://manualzz.com/doc/10893627/kaco-02xi-and-02x-grid-tied-inverter>
- [57] *GE GEPVe 3000-NA-240 Inverter*, <http://www.solardesignstool.com/components/inverter-grid-tie-solar/GE/478/GEPVe-3000-NA-240/specification-data-sheet.html?jsessionid=1472F79978D5560586974C6B7A658EBD> (accessed: October 2021).
- [58] *Fronius USA, LLC IG Plus IG Plus 6.0-1 UNI [240V], inverter datasheet, Fronius.*, available on [October 2021], <https://www.energysage.com/solar-inverters/fronius-usa-llc/1049/ig-plus-60-1-uni/>.
- [59] *SunPower SPR-12000 SPR-12000f [240V], inverter datasheet, Sunpower*, available on [October 2021], <https://www.energysage.com/solar-inverters/sunpower-corporation/2837/spr-12000f/>.
- [60] *Performance ratio; Quality factor for the PV plant, Technical information, SMA Solar Technology AG*, available on [October 2021], <https://files.sma.de/downloads/Perfratio-TI-en-11.pdf>.
- [61] A. Smets, K. Jäger, O. Isabella, R. van Swaaij, M. Zeman, *Solar Energy: The Physics and Engineering of Photovoltaic Conversion Technologies and System*, UIT Cambridge, Cambridge **2015**.
- [62] T. Blom, A. van den Dobbelsteen, *CO2-Roadmap TU Delft*, Campus & Real Estate, TU Delft **2019**.
- [63] N. Haala, M. Kada, *ISPRS J. Photogramm. Remote Sens.* **2010**, 65, 570.
- [64] Y. Xiao, C. Wang, X. H. Xi, W. M. Zhang, *IOP Conf. Ser. Earth Environ. Sci.* **2014**, 17.
- [65] H. Ledoux, F. Biljecki, B. Dukai, K. Kumar, R. Peters, J. Stoter, T. Commandeur, J. *Open Source Software* **2021**, 6, 2866.